AIAA JOURNAL
Vol. 46, No. 1, January 2008

High-Order-Accurate Numerical Method for Complex Flows

A. Gross* and H. F. Fasel†
University of Arizona, Tucson, Arizona 85721

DOI: 10.2514/1.22742

A numerical method employing high-order-accurate (higher than third) upwind discretizations for solving the compressible Navier–Stokes equations on structured grids is discussed. The inviscid fluxes are computed by a procedure based on a weighted essentially nonoscillatory interpolation of the characteristic variables and the Roe scheme. Application of the numerical method to a number of test cases of increasing complexity, that are prototypical for several of the key aspects of practical flows, demonstrates the accuracy and robustness of the method even when computing on distorted curvilinear grids. Significant reductions in computer time are possible when a second-order-accurate implicit Adams–Moulton scheme is employed for time integration. The combination of implicit time integration and high-order-accurate spatial discretization is shown to lead to significant savings in compute time as the grid resolution requirement is lowered and the time step can be increased.

Nomenclature

A	=	cell face area, amplitude of fundamental
$\mathbf{A}$	=	Jacobian of convective flux vector
C	=	vortex strength
c	=	speed of sound
E	=	parallel efficiency, error
e	=	energy
F	=	flux vector
H	=	residual vector
h	=	total enthalpy
I, J	=	number of cells in x and y
i, j, k	=	grid line indices
J	=	Jacobian of coordinate transformation, cell volume
M	=	Mach number
Q	=	state vector
q	=	vector of linearization variables
$\mathbf{R}$	=	right eigenvector matrix of $\mathbf{A}$
r	=	width of smoothness estimator stencils, radius
T	=	temperature
t	=	time
u	=	x velocity
V	=	contravariant velocity
v	=	velocity, y velocity
W	=	vector of characteristic variables
x, y, z	=	coordinates
γ	=	isentropic exponent
$\mathbf{\Lambda}$	=	eigenvalue matrix of $\mathbf{A}$
μ	=	viscosity
ξ	=	curvilinear coordinate
ρ	=	density

Subscripts

i, j, k	=	coordinate indices
w	=	wall
∞	=	freestream or inlet conditions

Superscripts

L	=	left side of cell face
n	=	time step
R	=	right side of cell face
v	=	viscous
ν	=	iteration index

Introduction

RECENTLY, the consideration of unsteady flow dynamics has become a more and more important aspect of computational fluid dynamics (CFD) for flows of technological relevance. This is especially the case because computers have now become powerful enough to allow for time-accurate three-dimensional computations for more complex geometries. Although the flowfield around complex geometries can be discretized in many ways (e.g., unstructured and structured body-fitted grids, immersed boundary techniques [1]), the geometrical complexity does in most instances complicate or deteriorate the accuracy of the respective method employed for solving the governing equations. Numerical techniques developed for simple geometries (e.g., Cartesian coordinates or cylindrical coordinates) do not necessarily keep their properties when applied to curvilinear grids and complex geometries. However, reasonably accurate results are still possible even on highly distorted grids when high-order-accurate (defined here to be higher than third) discretizations are employed [2].

As high Reynolds number flows require an extremely fine clustering of grid points near solid surfaces, solving the governing equations on body-fitted grids appears to be one of the most efficient approaches for computing flows around complex geometries. The use of structured grids simplifies the numerical treatment and allows for more efficient line relaxation methods. In general, for complex geometries, locally highly distorted grids must be expected. This requires numerical schemes that preserve the conservation properties of the governing equations and the finite volume approach seems to be the natural choice.

Another general concern is to develop codes that are more versatile and suited for a broader range of flow regimes without a significant loss of computational efficiency. This implies solving the full compressible Navier–Stokes equations in conservative form with numerical methods that perform equally well at subsonic and supersonic speeds. Because shock waves can be expected for transonic and supersonic flows, the use of upwind schemes appears natural. Another favorable property of upwind schemes is the damping of spurious numerical oscillations, especially in areas of high grid distortion. For high-order accuracy, weighted essentially nonoscillatory (WENO) schemes [3–6] may be employed. Although the high-order accuracy of the WENO schemes lowers the grid resolution requirement they are computationally more expensive.

Presented as Paper 2735 at the 32nd AIAA Fluid Dynamics Conference, St. Louis, MO, 24–26 June 2002; received 25 January 2006; revision received 26 September 2007; accepted for publication 26 September 2007.

*Research Assistant Professor, Department of Aerospace and Mechanical Engineering. Member AIAA.

†Professor, Department of Aerospace and Mechanical Engineering. Member AIAA.

Implicit time-integration schemes allow for larger time steps than explicit schemes and can lower the computational cost. Implicit methods based on the finite volume formulation and second-order-accurate upwind schemes, such as the CFL3D code [7,8], are commonly used today. However, as simulations of unsteady flows become increasingly more important for engineering applications, research is also directed toward the use of high-order-accurate numerical methods for lowering the computational cost. A high-order-accurate compressible code in a finite difference formulation and for curvilinear coordinates was developed by Visbal and Gaitonde [2] for computing unsteady compressible subsonic flows. The code employs high-order-accurate compact differences and implicit filters.

The computational method described herein is based on an earlier method by Schröder and Hartman [9] and Weiland et al. [10]. This earlier method was geared toward computing steady-state solutions of the compressible thin-layer Navier–Stokes equations in curvilinear coordinates. Toward this end, a Newton relaxation scheme in conjunction with upwind approximations to the flux Jacobians in the implicit operator was employed. The method was based on a finite volume formulation, where the fluxes were computed by second-order-accurate upwind schemes [a modified version of Leer's flux vector splitting scheme [11] and a symmetric total variation diminishing (TVD) scheme [12]].

In the present approach, to increase the accuracy of the spatial discretization while keeping the upwind properties and thereby the capability to compute flows with discontinuities, the convective fluxes are computed with high-order-accurate upwind schemes based on a WENO interpolation [3–6] of the characteristic variables and the Roe scheme [13]. Alternatively, the convective fluxes can be computed with a second-order-accurate symmetric TVD scheme [12] or split difference stencils [14,15]. The viscous terms are computed using high-order-accurate finite difference or finite volume approximations. Either, a second-order-accurate implicit Adams–Moulton (AM) method [16] or a fourth-order-accurate explicit Runge–Kutta (RK) method [17] are employed for time-accurate computations. The method was generalized to allow for multiple computational subdomains and parallelization using the message passing interface (MPI) software.

In the following the governing equations are introduced and the discretization techniques and boundary conditions are explained. The properties of the numerical method are explored in a number of test cases of increasing complexity. These range from a vortex convection test case to the more complicated problem of a laminar separation bubble on the suction side of a low-pressure turbine blade.

Numerical Method

The governing equations are the compressible Navier–Stokes equations in curvilinear coordinates ξ_i $(i = 1, 2, 3)$

$$J\frac{\partial Q}{\partial t} + \frac{\partial F_i}{\partial \xi_i} = \frac{1}{Re}\frac{\partial F_i^v}{\partial \xi_i} \tag{1}$$

The equations are nondimensionalized by a reference length L, velocity v_∞, density ρ_∞, and viscosity μ_∞. $Re = \rho_\infty v_\infty L/\mu_\infty$ is the Reynolds number and J is the Jacobian of the transformation from physical x_i $(i = 1, 2, 3)$ to curvilinear coordinates ξ_i. The state vector is $Q = [\rho \;\; \rho v_1 \;\; \rho v_2 \;\; \rho v_3 \;\; \rho e]^T$ with velocities v_i in the x_i direction, density ρ, and total energy $e = \varepsilon + e_{\text{kin}}$, where ε is the internal energy and $e_{\text{kin}} = 1/2 v_i v_i$ is the kinetic energy. Only perfect gases are considered. The equation of state is $p = \rho T/\gamma M_\infty^2$ with static pressure p and temperature T. The isentropic exponent is $\gamma = 1.4$ and M_∞ is the reference Mach number $M_\infty = v_\infty/c_\infty$. The local speed of sound is $c = \sqrt{T}/M_\infty$, the internal energy is $\varepsilon = T/[\gamma(\gamma - 1)M_\infty^2]$ and the total enthalpy is $h = e + p/\rho$. F_i and F_i^v are the convective and viscous flux vectors. The contravariant velocities are $V_i = \xi_{i,j} v_j$. The metric terms are $\xi_{i,j} = J\partial \xi_i/\partial x_j$. The laminar viscosity μ is computed from Sutherland's law,

$$\frac{\mu}{\mu_\infty} = T^{1.5}\frac{1 + 0.5}{T + 0.5} \tag{2}$$

The thermal conductivity is computed from the Prandtl analogy $\kappa = \mu/[Pr(\gamma - 1)M_\infty^2]$ with constant Prandtl number, Pr.

Spatial Discretization

The physical space is discretized by structured grids that are organized in i, j, and k ($i = 0 \cdots I$, etc.). For the computation of the cell volume, J, and the cell face areas, A_i, the cell edges are assumed to be straight and the cell faces are assumed to be planar. The method described herein was developed mainly for the application to flows over complex geometries where highly distorted grids are expected to be the rule and not the exception. For robustness and because of its conservation properties, the method was laid out as a finite volume method. Additional numerical stability can be achieved when the convective terms are discretized with upwind schemes such as the Roe scheme [13],

$$F_{i+\frac{1}{2}} = \frac{F_{i+1} + F_i}{2} - |\mathbf{A}_{i+\frac{1}{2}}|\frac{Q_{i+1} - Q_i}{2} \tag{3}$$

Here, $\mathbf{A} = \partial F/\partial Q = \mathbf{R}\boldsymbol{\Lambda}\mathbf{R}^{-1}$ is the Jacobian of the flux vector, and $|\mathbf{A}| = \mathbf{R}|\boldsymbol{\Lambda}|\mathbf{R}^{-1}$. $\mathbf{R}$ is the matrix of right eigenvectors and $\boldsymbol{\Lambda}$ is the eigenvalue matrix of $\mathbf{A}$. These matrices can be found in the Appendix. The transformation from differences of the conservative variables to differences of the characteristic variables is $\delta W = \mathbf{R}^{-1}\delta Q$. All matrices were computed from quantities at the cell face $i + 1/2$ which were computed by Roe averaging quantities from i and $i + 1$. This widely used approach affects the order of the scheme only indirectly as the matrices employed for the forward and backward transformations are computed from the same averages. For unsteady flow simulations, high-order accuracy is sought. The flow variables are reconstructed at the left (L) and right side (R) of the $i + 1/2$ interface using high-order-accurate WENO approximations [3–6]. The Roe scheme is then applied to L and R instead of i and $i + 1$. First, the differences of the characteristic variables are computed $\Delta W_{k+(1/2)} = \mathbf{R}^{-1}_{i+(1/2)}(Q_{k+1} - Q_k)$, where $k = i - r + 1, \ldots, i + r - 1$. When the $\mathcal{O}(5)$ WENO approximation $[r = 3, \mathcal{O}(2r - 1) = \mathcal{O}(5)]$ is employed, the left and right states are obtained from

$$Q^L_{i+\frac{1}{2}} = \frac{1}{12}(-Q_{i-1} + 7Q_i + 7Q_{i+1} - Q_{i+2}) - \mathbf{R}_{i+\frac{1}{2}}\varphi_N(\Delta W_{i-\frac{3}{2}}, \Delta W_{i-\frac{1}{2}}, \Delta W_{i+\frac{1}{2}}, \Delta W_{i+\frac{3}{2}}) \tag{4}$$

$$Q^R_{i+\frac{1}{2}} = \frac{1}{12}(-Q_{i-1} + 7Q_i + 7Q_{i+1} - Q_{i+2}) + \mathbf{R}_{i+\frac{1}{2}}\varphi_N(\Delta W_{i+\frac{5}{2}}, \Delta W_{i+\frac{3}{2}}, \Delta W_{i+\frac{1}{2}}, \Delta W_{i-\frac{1}{2}}) \tag{5}$$

which is a central interpolation

$$\sum_{k=i-r+2}^{i+r-1} c_k Q_k \tag{6}$$

combined with a WENO part

$$\varphi_N(a_0, a_1, \ldots, a_{2r-3}) \tag{7}$$

that is applied individually to each element of the ΔW vector. Here and in the following, the formal order of accuracy is denoted by $\mathcal{O}(\,)$. Further details and coefficients for the $\mathcal{O}(5)$ scheme and $\mathcal{O}(7)$ and $\mathcal{O}(9)$ schemes can be found in [18]. For comparison, a $\mathcal{O}(2)$ symmetric TVD upwind scheme was implemented [Harten and Yee upwind scheme (modified flux approach) with van Leer limiter as described by Yee [12], page 21]. Also, as a reference, $\mathcal{O}(2)$ and $\mathcal{O}(4)$ split differences in conjunction with a predictor–corrector method for time integration were implemented [14,15]. For the split differences, the equations had to be solved in the finite difference formulation. This approach was found to be inappropriate for highly

distorted grids because it did not satisfy the conservation properties of the governing equations. Nevertheless, when the computational grid is equidistant, the finite difference and finite volume formulation become identical to each other.

The viscous terms are computed using a shifted control volume approach or standard finite differences. For the latter, whenever derivatives are taken of derivatives (second derivatives are computed by integration by parts) the combined resulting stencil must not become wider than required by the accuracy [three points for $\mathcal{O}(2)$ and five points for $\mathcal{O}(4)$ accuracy]. Otherwise, numerical oscillations were observed to arise. By choosing the appropriate one-sided stencils for the "inner" derivatives the resulting stencil width can be kept minimal. In the following, the finite volume viscous terms are denoted by FV and the finite difference viscous terms are denoted by FD. For the split differences and the FD viscous terms, the metric terms at the cell centers are computed by a $\mathcal{O}(3)$ interpolation, $\xi_i = 1/16(-\xi_{i-(3/2)} + 9\xi_{i-(1/2)} + 9\xi_{i+(1/2)} - \xi_{i+(3/2)})$.

Temporal Integration

The Navier–Stokes equations can be cast into the form

$$\frac{\partial Q}{\partial t} = \tilde{F} \tag{8}$$

where $\tilde{F}$ is the sum of all flux vector differences divided by the Jacobian J. Three time-integration methods were implemented, a $\mathcal{O}(4)$ explicit RK method [17],

$$Q_1 = Q^n + \frac{\Delta t}{2}\tilde{F}(Q^n) \tag{9}$$

$$Q_2 = Q^n + \frac{\Delta t}{2}\tilde{F}(Q_1) \qquad Q_1 \Leftarrow Q_1 + 2Q_2 \tag{10}$$

$$Q_2 = Q^n + \Delta t\tilde{F}(Q_2) \qquad Q_1 \Leftarrow \frac{1}{3}(-Q^n + Q_1 + Q_2) \tag{11}$$

$$Q^{n+1} = Q_1 + \frac{\Delta t}{6}\tilde{F}(Q_2) \tag{12}$$

which was found to be stable up to Courant–Friedrich–Lewis (CFL) numbers of 1, the $\mathcal{O}(2)$ implicit AM method [16],

$$\frac{2}{\Delta t}(Q^{n+1,\nu} - Q^n) - (\tilde{F}^{n+1,\nu} + \tilde{F}^n) = 0 \tag{13}$$

and the $\mathcal{O}(1)$ Euler backward method [16],

$$\frac{1}{\Delta t}(Q^{n+1,\nu} - Q^n) - \tilde{F}^{n+1,\nu} = 0 \tag{14}$$

For the two latter methods, which are unconditionally stable for the $y' = \alpha y$ model equation, the new time step is approached iteratively. The residual H of Eqs. (13) and (14) is reduced by performing Newton–Raphson steps,

$$\left.\frac{\partial H}{\partial q}\right|^{n+1,\nu} \Delta q = -H^{n+1,\nu} \tag{15}$$

with iteration index ν where $q = [p \;\; v_1 \;\; v_2 \;\; v_3 \;\; T]^T$. The resulting system of equations is solved by a line Gauss–Seidel method based on a block Thomas algorithm [16] and the state vector is updated by $q^{n+1,\nu+1} = q^{n+1,\nu} + U\Delta q$, with underrelaxation factor $0 < U \leq 1$. The convergence of the iterative procedure is monitored by considering the individual components, H_m, of the residual vector, H, for all cells N,

$$R = \max_m(R_m) \quad \text{where } R_m = \sqrt{\frac{1}{N}\sum_N H_m^2} \tag{16}$$

The CFL number,

$$\text{CFL} = \frac{\Delta t}{J}\max_{i=1,2,3}(|V_i| + A_i c) \tag{17}$$

is computed from the time step, Δt.

Boundary Conditions

The physical space is decomposed into multiple computational subdomains where different boundary conditions and domain interconnections can be specified locally for every boundary cell. Instead of one-sided difference stencils and truncated WENO schemes, the ghost cell approach was applied at all boundaries. The resulting adiabatic wall boundary condition does not directly enforce the no-slip condition, $v_i = 0$, and is only first order accurate. The ghost cell approach does, however, allow for an accurate treatment of slip walls and interdomain boundaries. For supersonic flow all quantities are specified at the inflow boundary and extrapolated into the ghost cells (assuming zero second derivatives) at the outflow boundary. For subsonic flow two boundary conditions are employed. For steady-state computations the following procedure is applied: At the inflow boundary, the static pressure is extrapolated (assuming zero first derivatives) and all other quantities are specified. At the outflow boundary, the static pressure is set to the freestream value and all other quantities are extrapolated assuming zero second derivatives. At the freestream boundary all quantities are extrapolated assuming zero first derivatives. For time-dependent problems a characteristics based boundary condition is employed at all boundaries [19].

Parallelization

Because the physical space is decomposed into a number of computational subdomains, one may choose to assign each subdomain to an individual processor. However, this does not guarantee optimal load balancing between the processors. Also, the number of subdomains has to match the number of processors. To guarantee a better load balancing and since few but large computational subdomains are expected, each subdomain is split up by the number of processors such that the interface area between the sub-subdomains is minimized. The MPI package was chosen for parallelization. When the explicit time-integration method is employed the flow data at the sub-subdomain boundaries are exchanged between the processors after each substep. When the implicit time-integration method is employed, the line Gauss–Seidel method is applied individually to each sub-subdomain and the Δq and Q at the sub-subdomain boundaries are lagged and swapped between the processors after each iteration.

Results

Inviscid Vortex Convection Problem

The vortex convection test case was employed for studying the degradation of the numerical accuracy due to grid distortion [2] and for estimating the accuracy of the discretization of the convective terms. This case was computed on three different types of grids, a "smooth" grid, a "single-warped," and a "double-warped" grid at three different resolutions (fine grid 771×257 cells, medium grid 387×129 cells, and coarse grid 195×65 cells). The extent of the computational domain was $-10 \cdots 50$ in the x direction and $-10 \cdots 10$ in the y direction. The smooth grids were Cartesian. For the distorted grids the displacements

$$x \Leftarrow x + \sin\left(\frac{2y}{5}\pi + 3\frac{x-10}{40}\pi\right) \tag{18}$$

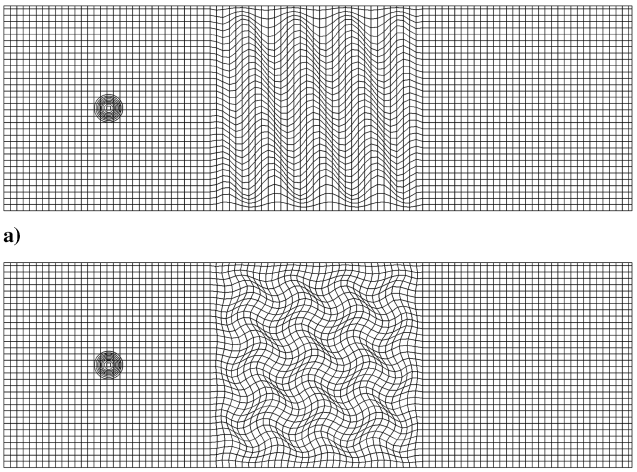

a)

b)

Fig. 1 Vortex convection: a) single- and b) double-warped coarse grid (every other line shown) with vorticity contour lines of initial condition superimposed.

$$y \Leftarrow y + \sin\left(\frac{2x}{5}\pi + 3\frac{y+10}{40}\pi\right) \tag{19}$$

were superimposed on the Cartesian grids and ramped in over a distance of 2.5 from all sides in the interval $x = 10 \cdots 30$. For the single-warped grid only the y coordinate was distorted while both coordinates were distorted for the double-warped grid. Visual inspection of the resulting grids (Fig. 1) may lead to the conclusion that the total distortion is lower for the latter. The properties of the viscous fluxes are not tested as the problem is inviscid. For the same reason, the spatial extent of the computational domain can be kept small as the vortex remains confined. The viscous terms were deactivated by setting the Reynolds number to 10^{30}. The Mach number was 0.1. The initial condition was [2]

$$u = u_\infty - yC\exp\left(\frac{-r^2}{2}\right) \qquad v = v_\infty + xC\exp\left(\frac{-r^2}{2}\right)$$
$$p = p_\infty - \frac{C^2\rho}{2}\exp(-r^2) \tag{20}$$

with $r = \sqrt{x^2 + y^2}$ and $C = 10^{-4}$. The temperature was assumed to be constant. Using the $\mathcal{O}(4)$ RK time-integration scheme and a time step of $\Delta t = 5 \times 10^{-3}$ the vortex was convected in the x direction over a distance of $\Delta x = 40$. This time step was found small enough for the accuracy of the time-integration scheme to have a negligible effect on the overall accuracy of the solution.

Results obtained using the coarse Cartesian grid are compared in Fig. 2 (left). Shown are u-velocity distributions taken at $t = 40$ and $x = 40$. Also included is the initial condition which is denoted as "reference." As there is no viscous dissipation, the vortex should not be dissipated and the velocity profile of the initial condition should be maintained. For the coarse grid, both the results obtained with the $\mathcal{O}(7)$ and $\mathcal{O}(9)$ WENO schemes still follow the reference very well, whereas the $\mathcal{O}(4)$ split differences and the $\mathcal{O}(5)$ WENO scheme are beginning to show some amplitude error. The second-order-accurate schemes exhibit a considerable amplitude error.

Results for the distorted grids are shown in Fig. 2 (center and right). Numerical stability issues prohibit the use of split differences. Although the error is clearly larger than on the Cartesian grid, both intensity and shape of the vortex are still somewhat accurately preserved for the $\mathcal{O}(7)$ and $\mathcal{O}(9)$ WENO schemes. The single-warped grid appears to have a more detrimental effect on the quality of the solution than the double-warped grid. Clearly, high-order-accurate schemes are needed for computing vortical structures on distorted grids with sufficient accuracy.

The total error of the u-velocity distributions at $t = 40$ and $x = 40$ was computed from

$$E = \sqrt{\frac{1}{J}\sum_j (u_j - u_{\text{reference}})^2} \tag{21}$$

When the error is plotted versus the grid resolution Δx (Fig. 3) and its distribution is approximated by $E = C\Delta x^n$, then n is the estimated accuracy of the discretization. The estimated accuracy is consistently lower than the formal accuracy. For the WENO $\mathcal{O}(9)$ scheme the numerical error is already leveling off on the fine grid. All cases were computed on one Alpha EV7 processor on a HP GS1280 (although, here only relative compute times are of interest). Figure 4 shows the dependency of the error on the compute time. If highly accurate solutions are required (low error) then the high-order-accurate WENO schemes have a clear advantage over the low-order-accurate TVD scheme and the split differences. Because all results were computed with the same time step, additional savings are possible for the high-order-accurate schemes because (for a constant CFL number) the time step can be increased when computing on coarser grids.

Grid distortion significantly lowers the estimated accuracy (Fig. 3, center and right). The drop-off in error (and hence the computed order of accuracy) is larger for the double-warped grid except for the WENO $\mathcal{O}(9)$ scheme where the general trend is reversed. Fourth-order accuracy is still maintained with the $\mathcal{O}(7)$ and $\mathcal{O}(9)$ WENO schemes. These results indicate that high-order-accurate schemes are necessary for maintaining a low overall error of the solution on distorted grids. Structured computational grids can feature areas of relatively low grid distortion (but high grid stretching) near the wall and areas of high grid distortion in the freestream. If the goal is to accurately capture unsteady flow structures (vortices) in areas with high grid distortion and low grid resolution, then the use of high-order-accurate schemes appears to be highly justified. The present

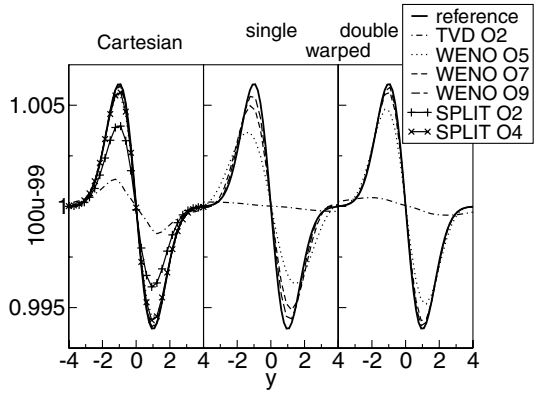

Fig. 2 Vortex convection: profiles of u velocity for Cartesian, single-warped, and double-warped coarse grid.

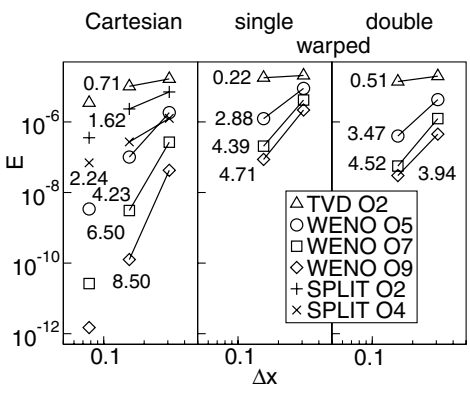

Fig. 3 Vortex convection: error of u-velocity profiles. Computed order of accuracy as indicated.

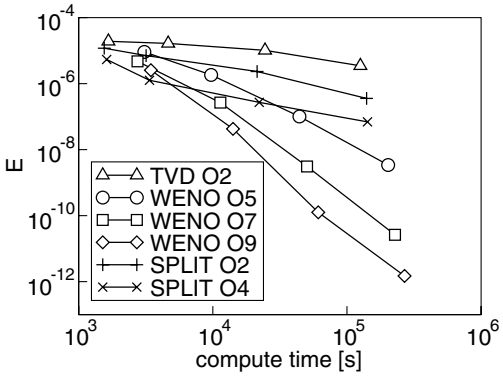

Fig. 4 Vortex convection: error of u-velocity profiles against compute time for Cartesian grids.

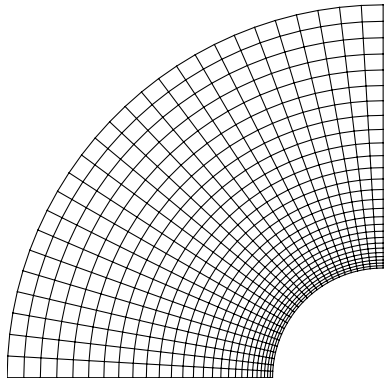

Fig. 6 Circular cylinder: coarse computational grid.

test case (vortex convection) was chosen because it scrutinizes this specific problem.

Inviscid Shock-Rarefaction Problem

The problem of a traveling shock wave followed by an isotropic expansion was chosen for studying how well the different schemes handle discontinuities and maintain amplitude and phase. Viscous effects were suppressed by setting the Reynolds number to $Re = 10^{30}$. A fine grid with 1500 and a coarse grid with 150 equidistantly spaced cells in the downstream direction $0 < x < 150$ were used. The problem is defined as follows. For $t < 0$ the fluid is at state 1, defined by $M_1 = 1.1$. For $0 \le t \le 2.5$ state 2 is prescribed at the inflow boundary, generating a shock wave that travels at $M_s = 2.2$. For $t > 2.5$ state 1 is once again prescribed at the inflow, resulting in an expansion fan that travels in the downstream direction. All cases were computed until $t = 60$. At that time instant the shock is positioned at $x = 120$ and the expansion fan is between $x = 109.8$ and 119.8. The equations were integrated in time with the $\mathcal{O}(4)$ RK method and a time step of $\Delta t = 0.01$. Fine grid results are shown in Fig. 5 (left). Results obtained with the upwind schemes are very close to the analytical solution. Although the split differences give rise to strong numerical oscillations, the result obtained with the $\mathcal{O}(4)$ split differences is still in reasonably good agreement with the analytical solution. Coarse grid results are shown in Fig. 5 (right). With split differences, numerical oscillations developed that completely destroyed the solution. The degree to which the upwind schemes preserve shape and amplitude of the analytical solution clearly depends on their respective accuracy.

Circular Cylinder in Supersonic Flow

We studied case 3 by Kopriva [20]. The reference conditions are as follows: Reynolds number (based on diameter) 3475, Mach number 5.97, Prandtl number 0.77, and freestream temperature 36.94 K. All cases were computed with the $\mathcal{O}(4)$ RK method and a time step of $\Delta t = 10^{-3}$. The results shown are at a nondimensional time of $t = 40$ after initialization of the flow with the freestream data. We employed two computational grids: A fine grid with 81×81 cells and a coarse grid with 27×27 cells that was obtained from the fine grid by coalescing boxes of 3×3 cells into single cells (Fig. 6). Only the upwind schemes were found to be numerically stable enough for computing this flow. With split differences a strong "ringing" of the solution near the shock wave (discontinuity) was observed and a stable solution could not be obtained. With the upwind schemes a distortion of the shock wave close to the symmetry plane ($y = 0$) could be observed in some instances. Sanders et al. explain this phenomenon (also referred to as "carbuncle phenomenon") as a lack of cross diffusion of one-dimensional numerical schemes [21]. To alleviate this problem, the H correction by Sanders et al. [21] was employed. Alternatively, for the WENO schemes, we also employed the local Lax–Friedrichs (LLF) flux. For the LLF flux, instead of the local eigenvalues on the cell face, the maxima of the absolute eigenvalues over the local relevant range (the interval over which the stencils stretch) are employed [5,6]. This adds diffusion and stabilizes the solution. The result was also found to depend on the formulation of the viscous terms (FD or FV).

A comparison of the fine grid solutions obtained with the $\mathcal{O}(5)$ WENO scheme is given in Fig. 7. Shown are isocontour lines of the local Mach number, $M = M_\infty \sqrt{(u^2 + v^2)/T}$. Results obtained with the $\mathcal{O}(7)$ and $\mathcal{O}(9)$ WENO schemes are very similar and, therefore, not shown. The H correction is clearly improving the quality of the solution near the symmetry plane. A similar effect is accomplished with the LLF flux. The differences between the solutions computed with the FD and FV viscous terms are minimal. However, weak grid mesh oscillations in the solution near the shock indicate that these solutions are not fully steady state. Indeed, the residuals could be converged down to machine accuracy only with the $\mathcal{O}(2)$ TVD scheme with H correction. For all high-order-accurate schemes a slight oscillation of the shock wave was observed (despite the additional stabilizing diffusion added by the H correction and the

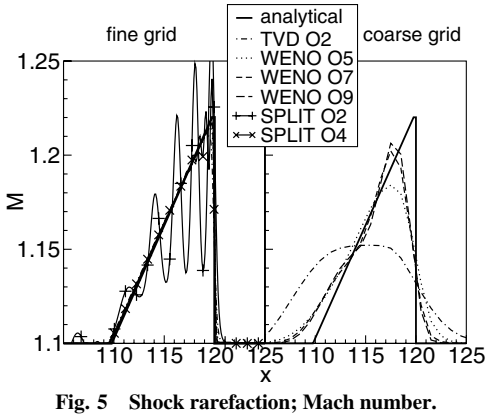

Fig. 5 Shock rarefaction; Mach number.

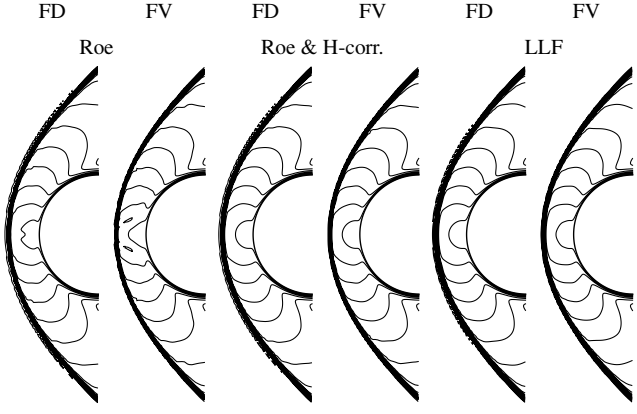

Fig. 7 Circular cylinder: isocontours of Mach number ($M = 0 \cdots 6$, $\Delta = 0.25$) computed with $\mathcal{O}(5)$ WENO scheme.

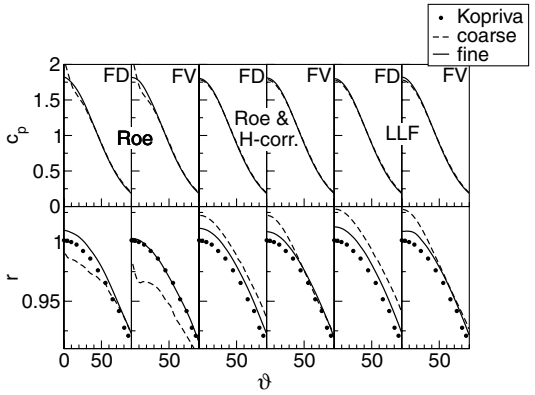

Fig. 8 Circular cylinder: wall pressure coefficient, c_p, and recovery factor, r; $\mathcal{O}(5)$ WENO results.

LLF flux). This observation was also made by Suresh and Huynh [22] for the oblique shock reflection problem, where the residual dropped only roughly 2 orders of magnitude when a $\mathcal{O}(5)$ WENO scheme was employed, but down to machine accuracy when a $\mathcal{O}(1)$ upwind scheme with upwind limiter was employed. Additional stabilizing methods, such as enforcing monotonicity preserving bounds on the reconstructed face values [5], are promising but were not explored. As the grid resolution is reduced the carbuncle phenomenon near the symmetry plane becomes more pronounced (not shown). Otherwise, despite a visual thickening of the shock wave (the number of cells in the shock is the same as for the fine grid) the results appear to be identical.

A comparison of the computed wall pressure coefficient distributions,

$$c_p = 2\left(p - \frac{1}{\gamma M_\infty^2}\right) \tag{22}$$

is shown in Fig. 8 (top). The variation in the wall pressure coefficient is minimal, except for the coarse grid results with the Roe flux (the cases with pronounced carbuncle phenomenon) where the stagnation point pressure is increased. A comparison of the computed recovery factor,

$$r = \frac{2(T_w - 1)}{(\gamma - 1)M_\infty^2} \tag{23}$$

with results by Kopriva [20], who employed a shock-fitted Chebyshev spectral method, are shown in Fig. 8 (bottom). The error in the recovery factor is always smaller than 3%. In most instances, the schemes are found to introduce energy into the flow at or near the shock, resulting in a larger recovery factor at the stagnation point. The best result is obtained with Roe flux and FV viscous terms. Both the H correction and the LLF flux increase the recovery factor. Finally, distributions of total enthalpy,

$$H = \frac{T}{(\gamma - 1)M_\infty^2} + \frac{1}{2}(u^2 + v^2) \tag{24}$$

in the symmetry plane ($y = 0$) for the TVD $\mathcal{O}(2)$ and WENO $\mathcal{O}(5)$ schemes are shown in Fig. 9. As the total enthalpy should remain constant over the shock wave, Fig. 9 helps estimate the conservation properties of the different schemes. With the FV viscous terms, the total enthalpy is conserved better across the shock. Both the

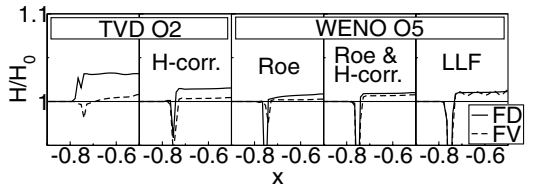

Fig. 9 Circular cylinder: total enthalpy at $y = 0$, fine grid results.

H correction and the LLF flux result in an increased postshock enthalpy.

Shear Layer

The disturbance amplification in a temporal shear layer was studied to test the accuracy of the viscous terms. This test case is similar but not identical to the case by Sandham and Reynolds [23]. A perfect match was not possible as the perturbation eigenfunction of the initial condition used in these earlier investigations was unknown. However, the same streamwise wave number of the fundamental disturbance, $\alpha = 0.71$, was chosen for the present studies. The dimensions of the computational domain are $x = -\pi/\alpha \cdots \pi/\alpha$ and $y = -5\pi/\alpha \cdots 5\pi/\alpha$. Only the x resolution was varied and the y resolution was kept constant (288 cells in y). Equidistant grid line spacing with 16, 32, and 64 cells in x and 96 cells in y was employed in the region $x, y = -\pi/\alpha \cdots \pi/\alpha$. In the regions $y = \pm(\pi/\alpha \cdots 5\pi/\alpha)$ a fifth-order polynomial grid stretching function was employed for distributing 96 cells in the y direction on either end such that the grid line spacing in the y direction over the entire domain was smooth. Periodicity conditions were prescribed at the inflow and outflow boundaries. The u-velocity profile was initialized with $u = \tanh(2y)$. As initial disturbance, a vortex [Eq. (20)] with $C = 10^{-5}$ and $r = 5\alpha/\pi\sqrt{x^2 + y^2}$ was superimposed on the initial condition. Reference Mach number, Reynolds number (based on initial vorticity thickness, $\delta_w = (u_2 - u_1)/(\partial u/\partial y)_{\max}$), and Prandtl number were 0.2, 400, and 1, respectively. The convective Mach number

$$M_c = \frac{u_2 - u_1}{c_2 + c_1} = \frac{u_2 - u_1}{\sqrt{T_2} + \sqrt{T_1}} M_\infty \tag{25}$$

was 0.2 with $u_1 = -u_2$ and $T_2 = T_1 = 300$ K. All cases were computed with the $\mathcal{O}(4)$ RK method and a time step of $\Delta t = 0.01$ over a time interval of 60.

A quantitative comparison of the results becomes possible when considering the shear layer momentum thickness,

$$\vartheta = \int \frac{u - u_1}{u_2 - u_1}\left(1 - \frac{u - u_1}{u_2 - u_1}\right) \mathrm{d}y \tag{26}$$

which was computed from the streamwise average using the second-order-accurate trapezoidal rule, and when considering the amplitude of the fundamental, A, which was computed by performing a Fourier transform in the x direction of the v velocity in the $y = 0$ plane. Results for the grid with 32 cells in x are shown in Fig. 10. The $\mathcal{O}(2)$ TVD scheme is found to be significantly more diffusive than all other schemes resulting in reduced growth rates.

As an analytical solution was unknown, the following procedure was employed for estimating the order of accuracy. Assuming that the discretization error can be expressed as

$$E = C\Delta x^n + D \tag{27}$$

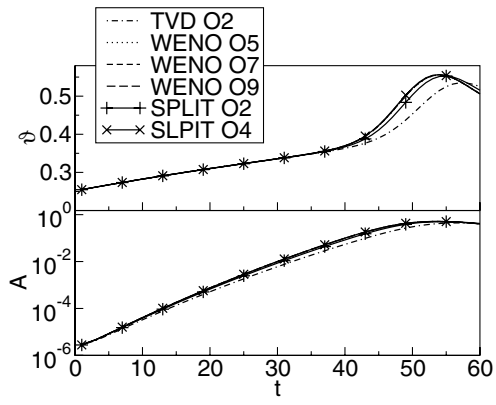

Fig. 10 Shear layer momentum thickness ϑ and amplitude of fundamental A.

and computing the difference between solutions on two different grids with grid line spacing, Δx_1 and Δx_2, the difference in error

$$\Delta E_{12} = C\left(\Delta x_2^n - \Delta x_1^n\right) = L_2(\cdots) \tag{28}$$

can be computed as some norm of the difference between the solutions. Here the L_2 and L_∞ norm of the amplitude of the fundamental, A, were chosen. With a third solution on a grid with grid line spacing, Δx_3, a second error difference ΔE_{13} can be computed. The order of the scheme, n, can then be computed from

$$\frac{\Delta E_{13}}{\Delta E_{12}} = \frac{\Delta x_3^n - \Delta x_1^n}{\Delta x_2^n - \Delta x_1^n} \tag{29}$$

Results are listed in Table 1. The computed order of accuracy for the WENO schemes is limited by the accuracy of the discretization of the viscous terms and close to 4. The split differences do not reach their formal order of accuracy. For the $\mathcal{O}(2)$ TVD scheme an estimated order of accuracy could not be computed as the error did not decrease monotonely with increasing grid resolution.

Compute times are listed in Table 2. All cases were computed on one Alpha EV7 processor on a HP GS1280. The high-order accuracy of the WENO schemes clearly comes at a cost. A direct comparison of compute time and achieved accuracy is impossible because the absolute error of the various results is unknown. The compute times for the $\mathcal{O}(2)$ and $\mathcal{O}(4)$ split differences are (for the current test case) approximately the same.

The combination of $\mathcal{O}(7)$ and $\mathcal{O}(9)$ schemes with $\mathcal{O}(4)$ viscous terms is only beneficial when the structures that are to be resolved are not much affected by viscosity. This is not the case here. The approach is, however, beneficial for simulations where sufficient grid resolution near the wall guarantees sufficient resolution in the viscous flow region near the wall, while a lack of accuracy away from the solid surfaces challenges the accuracy of the discretization of the convective terms. In such situations, high-order-accurate schemes allow one to capture more of the unsteady flow motion. Employing $\mathcal{O}(7)$ and $\mathcal{O}(9)$ schemes together with the $\mathcal{O}(4)$ viscous terms for resolving all length scales down to the Kolmogorov length scales makes little sense. The better approach then would be to employ the $\mathcal{O}(5)$ scheme in combination with the $\mathcal{O}(4)$ viscous terms or to employ even higher-order-accurate viscous terms (which were found to be very computationally expensive).

Adiabatic Fanno Flow

The adiabatic Fanno flow was computed to study how the low-order accuracy of the ghost cell wall boundary condition affects the accuracy of the solution. The dimensions of the computational domain were 1×0.005 with 100 evenly spaced cells in x and 9, 27, and 81 evenly spaced cells in y. The reference Mach number, Reynolds number (based on channel height h), and Prandtl number were 0.25, 100,000, and 0.72, respectively. The velocity profile of the incompressible Poiseuille flow, $u = 1 - 4(y/h)^2$, with $T = 1$ was prescribed at the inflow boundary. All cases were computed with

Table 1 Shear layer: estimated order of accuracy

Scheme	WENO $\mathcal{O}(5)$	$\mathcal{O}(7)$	$\mathcal{O}(9)$	SPLIT $\mathcal{O}(2)$	$\mathcal{O}(4)$
L_2	3.76	4.25	3.35	0.78	3.25
L_∞	3.58	4.37	3.60	0.80	2.81

Table 2 Shear layer: compute times in seconds

Cells	TVD $\mathcal{O}(2)$	WENO $\mathcal{O}(5)$	$\mathcal{O}(7)$	$\mathcal{O}(9)$	SPLIT $\mathcal{O}(2)$	$\mathcal{O}(4)$
16×288	309	656	776	972	226	236
32×288	626	1328	1552	1925	448	451
64×288	1355	2546	3173	3936	1034	1028

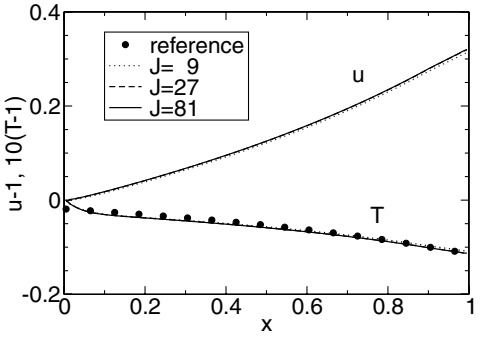

Fig. 11 Fanno flow: velocity and temperature profiles at $y = 0$; $\mathcal{O}(9)$ WENO results.

the $\mathcal{O}(1)$ Euler backward method and one iteraton per time step. The residuals dropped 2 orders of magnitude for the $\mathcal{O}(7)$ and $\mathcal{O}(9)$ WENO schemes and down to machine accuracy for the other schemes. With the split differences steady-state solutions could not be obtained. For adiabatic Fanno flow the temperature distribution

$$\frac{T}{T^*} = \frac{\gamma + 1}{2 + (\gamma - 1)M^2} \tag{30}$$

is coupled to the local Mach number distribution where the asterisk indicates the Laval condition ($M = 1$). By plugging the fine grid $\mathcal{O}(9)$ WENO Mach number distribution into Eq. (30) the reference curve in Fig. 11 was obtained. The overall order of accuracy, which was computed from profiles extracted at $x = 0.905$, is clearly limited to about 2 (Table 3). Keeping in mind that according to Gustafsson [24] the boundary conditions should be no more than 1 order less accurate than the interior scheme, the current results indicate that the ghost cell wall boundary condition is first order accurate.

Tollmien–Schlichting Wave

The amplification of Tollmien–Schlichting waves in a laminar boundary layer is crucially dependent on the accuracy of the wall boundary condition and the discretization. For the following test case the conditions documented in Sec. 5.3 (nonparallel base flow instability) in the paper by Wasistho et al. [25] were chosen. The Mach number was 0.5, the Reynolds number based on the inflow displacement thickness was $Re = 750$, and the nondimensional forcing frequency was 0.06. Different from Wasistho et al., the length scales were nondimensionalized such that the Reynolds number (based on an arbitrarily chosen reference length) was 100,000 resulting in a nondimensional forcing frequency of 1.2732. The freestream temperature was 300 K. The dimensions of the computational domain were 8.64×2.5 ($=L_y$) with 770 equidistantly spaced cells in x and 196 cells in y. The minimum y grid line spacing near the wall was $\Delta y_{\min} = 0.000231$. For the wall normal grid point distribution, y_j, a maximum thickness ratio (from one cell to the next) of $f_{\max} = 1.03$ was specified. A local thickness ratio dependent on the grid line index $j = 0 \cdots J$,

$$f_j = (f_{\max} - 1)\left(\frac{J - j}{J - 2}\right)^c + 1 \tag{31}$$

was then computed for each grid point and the parameter c was varied such that the series $y_0 = 0$, $y_1 = \Delta y_{\min}$, $y_j = y_{j-1} + (y_{j-1} - y_{j-2})f_j, \ldots$ satisfied the boundary condition $y_J = L_y$. A v-velocity disturbance was introduced through a forcing slot located between

Table 3 Computed order of accuracy

Scheme	TVD $\mathcal{O}(2)$	WENO $\mathcal{O}(5)$	$\mathcal{O}(7)$	$\mathcal{O}(9)$
$L_2(u)$	1.98	2.12	2.11	2.13
$L_2(T)$	1.96	2.71	2.69	2.71
$L_\infty(u)$	1.98	2.03	2.03	2.04
$L_\infty(T)$	1.96	2.55	2.52	2.59

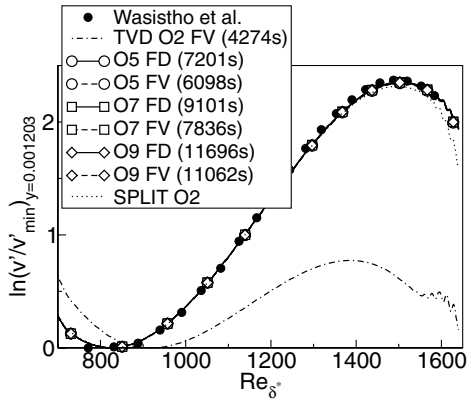

Fig. 12 Tollmien–Schlichting wave: *v*-disturbance amplitude (compute times in parentheses).

0.1122 and 0.3815 [17]. The disturbance amplitude was 10^{-5}. A compressible boundary layer similarity solution was prescribed as initial condition. For the present results, the base flow was first converged over a time interval of 39.27. Then the disturbance was introduced and the flow was computed over an additional time interval of 15.71. All reported wall clock compute times are for this second time interval. Simulations were run on 16 Itanium2 processors on a HP rx-5670. Finally, one period of the disturbance, 0.7854, was computed and the data were Fourier transformed in time to obtain the disturbance amplitudes.

A comparison of the v-velocity disturbance amplitude at $y = 0.001203$ normalized by its minimum value is shown in Fig. 12. All but the $\mathcal{O}(2)$ split difference result were computed with the $\mathcal{O}(2)$ AM method, a time step of $\Delta t = 0.007854$, $R = 10^{-6}$, and $U = 0.5$. The WENO results match the reference data by Wasistho et al. [25] very well. Although the discretization of the viscous terms (FD or FV) has a negligible influence on the results, it was found that the FD viscous terms require more compute time. The $\mathcal{O}(7)$ and $\mathcal{O}(9)$ schemes are about 29 and 81% more expensive than the $\mathcal{O}(5)$ scheme (with FV viscous terms). The result obtained with $\mathcal{O}(2)$ TVD scheme is clearly too diffusive, while the result obtained with $\mathcal{O}(2)$ split differences is approaching that of the high-order-accurate schemes. No compute time is given for the $\mathcal{O}(2)$ split differences as this case was computed with the RK method and a 100 times smaller time step. The physical x resolution was 26 cells per wavelength (Wasistho employed 24 grid points per wavelength). The result did not change noticeably when the disturbance amplitude was increased or decreased by a factor of 10 (not shown) indicating that the current simulations can be considered to be within the linear regime. Figure 13 illustrates that for $R < 10^{-2}$ the results are almost independent of R. About double the total compute time is required for $R = 10^{-6}$ when compared with $R = 10^{-1}$. We also studied the influence of the time step on the result.

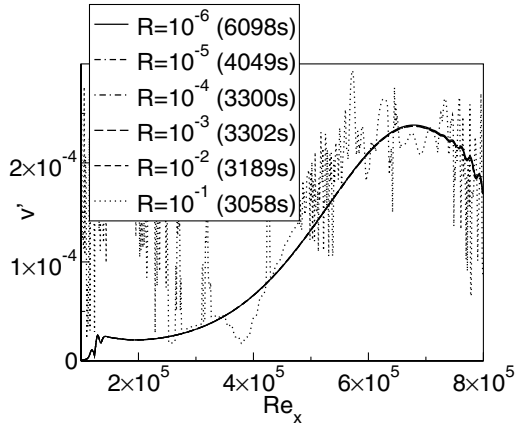

Fig. 13 Tollmien–Schlichting wave: *v*-disturbance amplitude (compute times in parentheses); $\mathcal{O}(5)$ WENO FV scheme.

For the implicit $\mathcal{O}(2)$ AM method with $\mathcal{O}(5)$ WENO (FV), a time step of $\Delta t = 0.007854$ (100 time steps per period, CFL = 69, 6098 s) is small enough for guaranteeing sufficient temporal resolution. At $\Delta t = 0.031416$ (25 time steps per period, CFL = 278, 2322 s) some minimal damping of the disturbance amplitude was detected near the outflow. However, the compute time was reduced by a factor of 2.6. Running the $\mathcal{O}(2)$ AM method at a small time step, $\Delta t = 0.0007854$ (1000 time steps per period, CFL = 6.9, 35105 s) is computationally wasteful. For larger time steps the implicit time integration has a clear advantage over the explicit $\mathcal{O}(4)$ RK time integration. The compute time required for the RK scheme with $\mathcal{O}(5)$ WENO (FV) at $\Delta t = 0.00007854$ (10000 time steps per period, CFL = 0.69, 31073 s) is 14 times larger than the compute time required for the $\mathcal{O}(2)$ AM method at $\Delta t = 0.031416$.

We also halved the number of cells in the streamwise direction resulting in a physical resolution of 13 cells per wavelength and shorter compute times. At this resolution the maximum disturbance amplitude was still predicted correctly by the $\mathcal{O}(7)$ and $\mathcal{O}(9)$ WENO schemes at a computational cost that was lower than for the finer grid with $\mathcal{O}(5)$ WENO scheme (4262 s and 5557 s versus 6098 s). We also found results that were obtained with half the near wall grid resolution, $2\Delta y_{\min}$, to still be sufficiently accurate. For these cases the implicit method was found to converge faster and additional savings became possible because the time step could be increased by a factor of 2.

Last, the influence of a moderate grid distortion on the result was studied. The equidistant grid was distorted in the following manner:

$$x \Leftarrow x - 0.05\left[1 - \cos\left(\frac{j}{J}\pi\right)\right]\sin\left(\frac{8i}{I}\pi\right) \tag{32}$$

$$\Delta y_{\min} \Leftarrow \Delta y_{\min}\left\{1 + 0.25\left[1 - \cos\left(\frac{8i}{I}\pi\right)\right]\right\} \tag{33}$$

The computed disturbance amplitude distributions were found to be virtually identical despite the grid distortion (not shown).

Linear Low-Pressure Turbine Cascade

As an example for one of the many possible applications of the method to more complex geometries, results from time-accurate numerical simulations of a PakB linear low-pressure turbine (LPT) cascade at a Reynolds number based on axial chord of 25,000 are shown. Simulations of such flows are particularly challenging due to the delicate interaction of separation and transition. Simulations were performed at two different grid resolutions and with two different schemes, the $\mathcal{O}(2)$ TVD scheme and the $\mathcal{O}(9)$ WENO scheme. The computational domain consisted of five blocks with a central O grid that wrapped around the blade. This block had a resolution of $500 \times 100 \times 64$ cells for the fine grid and half the resolution for the coarse grid. The y^+ value of the wall next grid points was below 1. All cases were computed with the $\mathcal{O}(2)$ AM method and a time step of $\Delta t = 0.0005$. Further details can be found in Gross and Fasel [26].

Instantaneous visualizations of the flow using the Q criterion are shown in Fig. 14. The Q criterion [27] indicates areas where rotation dominates strain. The boundary layer is laminar at the separation location, transitions in the separated flow region, and reattaches to the blade, enclosing (in the mean) a separation bubble. Figure 14 also clearly demonstrates that detail is lost on the coarser grid and for the less accurate $\mathcal{O}(2)$ TVD scheme.

A comparison of the time-averaged (all time averages were computed over a time interval of 40) wall pressure coefficient with measured data [28,29] is given in Fig. 15. The $\mathcal{O}(2)$ TVD fine grid and the $\mathcal{O}(9)$ WENO coarse and fine grid results seem to converge (despite a slightly earlier separation for the less accurate scheme) to a unique distribution which is in reasonable agreement with the experimental data. When considering wall normal profiles of total velocity, the thickness of the separation bubble at $x = 0.84$ and $x = 0.92$ appears underpredicted when compared with the experiment [28] (Fig. 16). Surprisingly, despite the poor agreement of the wall pressure distribution, the velocity profiles obtained with

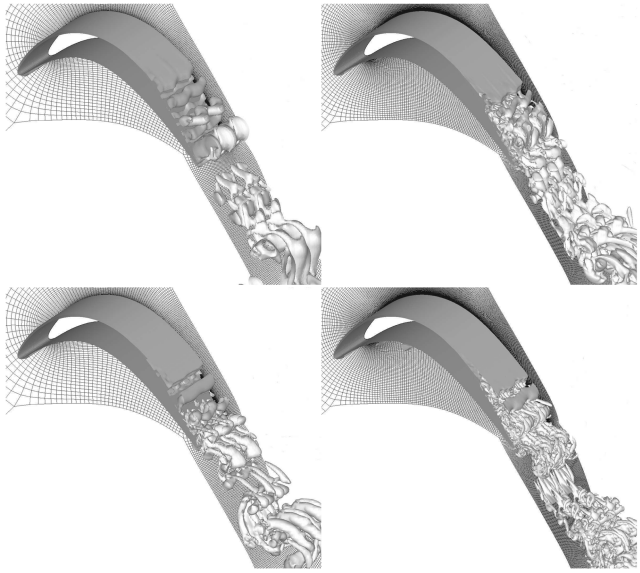

Fig. 14 Low-pressure turbine cascade: isosurfaces of $Q = 1$. Coarse (left) and fine grid (right) results obtained with $\mathcal{O}(2)$ TVD (top) and $\mathcal{O}(5)$ WENO scheme (bottom).

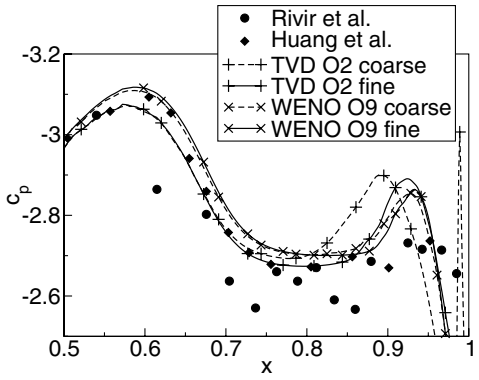

Fig. 15 Low-pressure turbine cascade: wall pressure coefficient.

the $\mathcal{O}(2)$ TVD scheme for the coarse grid are similar to the other profiles.

Finally, a comparison of the total wall clock time dependent on the case, the time-integration scheme and time step, and the number of processors is given in Fig. 17. All cases were computed on a Cray XD1 (AMD Opteron 275 processors). For the $\mathcal{O}(2)$ AM method, 10 time steps with $\Delta t = 5 \times 10^{-4}$ were computed with an underrelaxation factor of $U = 0.25$ and an iteration convergence criterion of $R = 1$. For the $\mathcal{O}(4)$ RK method, 2500 time steps with

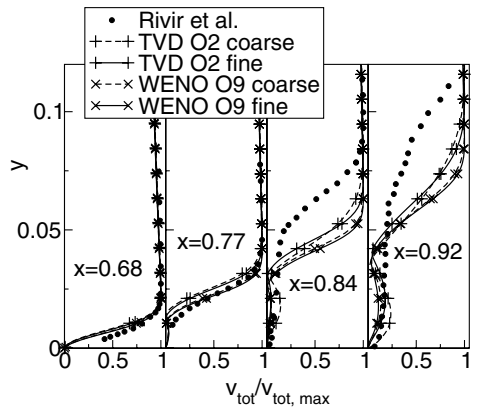

Fig. 16 Low-pressure turbine cascade: wall normal velocity profiles.

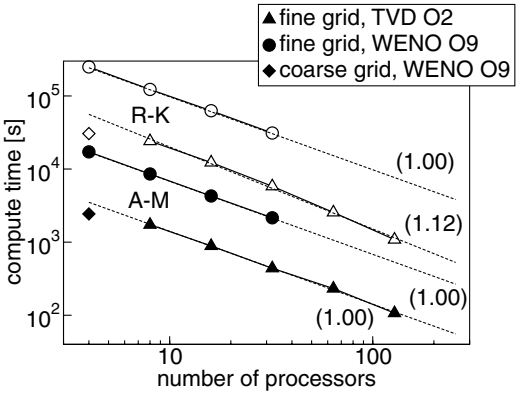

Fig. 17 Low-pressure turbine cascade; compute times in seconds; estimates for parallel efficiency in parentheses.

$\Delta t = 2 \times 10^{-6}$ were computed. The maximum CFL numbers were about 220 (fine grid, AM), 0.89 (fine grid, RK), 110 (coarse grid, AM), and 0.44 (coarse grid, RK). With the $\mathcal{O}(9)$ WENO scheme the number of iterations per time step was roughly 40 for the fine grid and 48 for the coarse grid. With the $\mathcal{O}(2)$ TVD scheme about 16 iterations were required per time step. Clearly, the implicit operator which was derived based on a $\mathcal{O}(1)$ upwind scheme discretization of the convective terms (resulting in a block-tridiagonal system; if higher accuracy of the implicit operator was desired the resulting system would have more nonzero bands) works less efficiently for the high-order-accurate scheme. Also, for larger numbers of processors, the line Gauss–Seidel algorithm loses some of its efficiency as more information is lagged at interprocessor boundaries. This was compensated for in the present calculations by lowering the underrelaxation factor resulting in more iterations per time step. In summary, additional savings are possible when computing on a coarser grid with less processors, a larger underrelaxation factor, and a larger time step. For the present results, both the underrelaxation factor and the time step were kept constant for all cases.

Figure 17 shows that the implicit time-integration results in compute time savings of more than 10. About 10 times more compute time is required with the high-order-accurate discretization when compared with the $\mathcal{O}(2)$ discretization. The compute time required for the coarse grid simulation is roughly 10 times less than the compute time required for the fine grid simulation (the ratio of the number of cells is 2.824 mil/0.35256 mil = 8). Considering that the coarse grid $\mathcal{O}(9)$ WENO result is of a similar quality as the fine grid $\mathcal{O}(2)$ TVD result and also considering that further savings are possible for the coarse grid (the time step can be increased by a factor of 2), the high-order-accurate discretization is clearly advantageous.

Finally, the parallel efficiency was estimated. If the wall clock time on p processors, T_p, is (through a data fit) expressed as $T_p = T_1/p^E$ where T_1 is the wall clock time on one processor, then E is a measure of the parallel efficiency (the customary definition of parallel efficiency, $E_p = T_1/(pT_p)$, is dependent on the number of processors). Figure 17 shows that linear speedup ($E = 1$) was accomplished in all instances except for the RK $\mathcal{O}(2)$ TVD fine grid case where, probably due to cash effects, super linear speedup was achieved.

Conclusions

A numerical method for solving the compressible Navier–Stokes equations on structured grids that employs both high-order-accurate upwind schemes and an implicit time-integration method is described in detail. Upwind schemes based on a WENO interpolation [3–6] of the characteristic variables and the Roe scheme [13] with a formal order of accuracy higher than 4 were incorporated to allow for stable and accurate simulations of unsteady compressible flows on distorted computational grids. These schemes were shown to effectively lower the grid resolution requirement for complex flow simulations and therefore lead to savings in total compute time. The

high-order-accurate WENO schemes were combined with an implicit second-order-accurate Adams–Moulton time-integration method which was demonstrated to lower the overall computational expense of the method by permitting larger time steps. Second- and fourth-order-accurate split differences, a second-order-accurate upwind TVD scheme, and a fourth-order-accurate explicit Runge–Kutta time-integration scheme were also included for comparison. The method was designed such that the computational domain can be decomposed into multiple subdomains. To achieve a good processor load balancing in multiprocessor computations, the computational subdomains are further split up into sub-subdomains according to the number of available processors.

Application of the method to a number of flow problems with increasing complexity demonstrated the basic properties of the method: Discontinuities can be computed stably without switching locally to lower-order schemes. The high-order schemes maintain good accuracy in areas with large grid distortion. This is essential when computing complex geometries with structured grids where grid distortion cannot always be avoided. Simulations of nonlinear disturbances in a temporal shear layer and of Tollmien–Schlichting waves in a laminar boundary layer demonstrated the ability of the method to accurately simulate time-dependent viscous flows. Finally, results for a linear low-pressure turbine cascade, which poses a particularly challenging problem as separation and transition interact, showed that the method was highly applicable for simulating complex time-dependent flows.

These examples clearly demonstrate that considerable gains with regard to accuracy and compute time are possible when employing high-order-accurate WENO based schemes in conjunction with an implicit time-integration method. This appears to be especially true when computing on distorted grids (as is often the case when complex geometries are "meshed" with structured grids) or when trans- and supersonic flows with embedded shocks are being considered.

Acknowledgments

This work was funded by the U.S. Air Force Office of Scientific Research (AFOSR) under Grant No. F9550-05-1-0166 and by the Office of Naval Research (ONR) under Grant No. N000014-01-1-09.

References

[1] Tseng, Y. H., and Ferziger, J. H., "A Ghost-Cell Immersed Boundary Method for Flow in Complex Geometry," *Journal of Computational Physics*, Vol. 192, No. 2, 2003, pp. 593–623. doi:10.1016/j.jcp.2003.07.024

[2] Visbal, M. R., and Gaitonde, D. V., "High-Order-Accurate Methods for Complex Unsteady Subsonic Flows," *AIAA Journal*, Vol. 37, No. 10, 1999, pp. 1231–1239.

[3] Liu, X. D., Osher, S., and Chan, T., "Weighted Essentially Nonoscillatory Schemes," *Journal of Computational Physics*, Vol. 115, No. 1, 1994, pp. 200–212. doi:10.1006/jcph.1994.1187

[4] Jiang, G. S., and Shu, C. W., "Efficient Implementation of Weighted ENO Schemes," *Journal of Computational Physics*, Vol. 126, No. 1, 1996, pp. 202–228. doi:10.1006/jcph.1996.0130

[5] Balsara, D. S., and Shu, C. W., "Monotonicity Preserving Essentially Non-Oscillatory Schemes with Increasingly High Order of Accuracy," *Journal of Computational Physics*, Vol. 160, No. 2, 2000, pp. 405–452. doi:10.1006/jcph.2000.6443

[6] Jiang, G. S., and Wu, C. C., "A High-Order WENO Finite Difference Scheme for the Equations of Ideal Magnetohydrodynamics," *Journal of Computational Physics*, Vol. 150, No. 2, 1999, pp. 561–594. doi:10.1006/jcph.1999.6207

[7] Thomas, J. L., Krist, S. T., and Anderson, W., "Navier-Stokes Computations of Vortical Flows over Low Aspect-Ratio Wings," *AIAA Journal*, Vol. 28, No. 2, 1990, pp. 205–212.

[8] Rumsey, C., Sanetrik, M., Biedron, R., Melson, N., and Parlette, E., "Efficiency and Accuracy of Time-Accurate Turbulent Navier-Stokes Computations," *Computers and Fluids*, Vol. 25, No. 2, 1996, pp. 217–236. doi:10.1016/0045-7930(95)00043-7

Appendix: Flux Vector Jacobian and Eigenvector Matrices

The derivative of the convective flux vector, F, with respect to the conservative variables, Q, is

$$\mathbf{A} = \frac{\partial F}{\partial Q} = \begin{bmatrix} 0 & \xi_{,1} & \xi_{,2} & \xi_{,3} & 0 \\ -v_1 V + (\chi + e_{\text{kin}}\kappa)\xi_{,1} & V + v_1\xi_{,1} - v_1\kappa\xi_{,1} & v_1\xi_{,2} - v_2\kappa\xi_{,1} & v_1\xi_{,3} - v_3\kappa\xi_{,1} & \kappa\xi_{,1} \\ -v_2 V + (\chi + e_{\text{kin}}\kappa)\xi_{,2} & v_2\xi_{,1} - v_1\kappa\xi_{,2} & V + v_2\xi_{,2} - v_2\kappa\xi_{,2} & v_2\xi_{,3} - v_3\kappa\xi_{,2} & \kappa\xi_{,2} \\ -v_3 V + (\chi + e_{\text{kin}}\kappa)\xi_{,3} & v_3\xi_{,1} - v_1\kappa\xi_{,3} & v_3\xi_{,2} - v_2\kappa\xi_{,3} & V + v_3\xi_{,3} - v_3\kappa\xi_{,3} & \kappa\xi_{,3} \\ (\chi + e_{\text{kin}}\kappa - h)V & -v_1 V\kappa + h\xi_{,1} & -v_2 V\kappa + h\xi_{,2} & -v_3 V\kappa + h\xi_{,3} & (1+\kappa)V \end{bmatrix}$$

with $h = (c^2 - \chi)/\kappa + e_{\text{kin}}$. For a perfect gas $\chi = 0$ and $\kappa = \gamma - 1$ [12]. The eigenmatrix of $\mathbf{A}$ is

$$\mathbf{\Lambda} = \text{diag}[\lambda_1, \lambda_2, \lambda_3, \lambda_4, \lambda_5] = \text{diag}[V, V, V, V + Ac, V - Ac]$$

The matrix of right eigenvectors of $\mathbf{A}$ is

$$\mathbf{R} = \begin{bmatrix} \tilde{\xi}_{,1} & \tilde{\xi}_{,2} & \tilde{\xi}_{,3} & 1 & 1 \\ v_1\tilde{\xi}_{,1} & v_1\tilde{\xi}_{,2} - c\tilde{\xi}_{,3} & v_1\tilde{\xi}_{,3} + c\tilde{\xi}_{,2} & v_1 + c\tilde{\xi}_{,1} & v_1 - c\tilde{\xi}_{,1} \\ v_2\tilde{\xi}_{,1} + c\tilde{\xi}_{,3} & v_2\tilde{\xi}_{,2} & v_2\tilde{\xi}_{,3} - c\tilde{\xi}_{,1} & v_2 + c\tilde{\xi}_{,2} & v_2 - c\tilde{\xi}_{,2} \\ v_3\tilde{\xi}_{,1} - c\tilde{\xi}_{,2} & v_3\tilde{\xi}_{,2} + c\tilde{\xi}_{,1} & v_3\tilde{\xi}_{,3} & v_3 + c\tilde{\xi}_{,3} & v_3 - c\tilde{\xi}_{,3} \\ (h - \frac{c^2}{\kappa})\tilde{\xi}_{,1} + c(v_2\tilde{\xi}_{,3} - v_3\tilde{\xi}_{,2}) & (h - \frac{c^2}{\kappa})\tilde{\xi}_{,2} + c(v_3\tilde{\xi}_{,1} - v_1\tilde{\xi}_{,3}) & (h - \frac{c^2}{\kappa})\tilde{\xi}_{,3} + c(v_1\tilde{\xi}_{,2} - v_2\tilde{\xi}_{,1}) & h + c\frac{V}{A} & h - c\frac{V}{A} \end{bmatrix}$$

with $\tilde{\xi}_{,j} = \xi_{,j}/A$, and its inverse is

$$\mathbf{R}^{-1} = \begin{bmatrix} \frac{1}{c}(v_3\tilde{\xi}_{,2} - v_2\tilde{\xi}_{,3}) - \tilde{\xi}_{,1}\frac{\kappa}{c^2}(2e_{\text{kin}} - h) & \frac{\tilde{\xi}_{,1}v_1\kappa}{c^2} & \frac{\tilde{\xi}_{,3}}{c} + \frac{\tilde{\xi}_{,1}v_2\kappa}{c^2} & -\frac{\tilde{\xi}_{,2}}{c} + \frac{\tilde{\xi}_{,1}v_3\kappa}{c^2} & -\tilde{\xi}_{,1}\frac{\kappa}{c^2} \\ \frac{1}{c}(v_1\tilde{\xi}_{,3} - v_3\tilde{\xi}_{,1}) - \tilde{\xi}_{,2}\frac{\kappa}{c^2}(2e_{\text{kin}} - h) & -\frac{\tilde{\xi}_{,3}}{c} + \frac{\tilde{\xi}_{,2}v_1\kappa}{c^2} & \frac{\tilde{\xi}_{,2}v_2\kappa}{c^2} & \frac{\tilde{\xi}_{,1}}{c} + \frac{\tilde{\xi}_{,2}v_3\kappa}{c^2} & -\tilde{\xi}_{,2}\frac{\kappa}{c^2} \\ \frac{1}{c}(v_2\tilde{\xi}_{,1} - v_1\tilde{\xi}_{,2}) - \tilde{\xi}_{,3}\frac{\kappa}{c^2}(2e_{\text{kin}} - h) & \frac{\tilde{\xi}_{,2}}{c} + \frac{\tilde{\xi}_{,3}v_1\kappa}{c^2} & -\frac{\tilde{\xi}_{,1}}{c} + \frac{\tilde{\xi}_{,3}v_2\kappa}{c^2} & \frac{\tilde{\xi}_{,3}v_3\kappa}{c^2} & -\tilde{\xi}_{,3}\frac{\kappa}{c^2} \\ \frac{1}{2c^2}[c^2 - c\frac{V}{A} + \kappa(2e_{\text{kin}} - h)] & \frac{1}{2c^2}(c\tilde{\xi}_{,1} - v_1\kappa) & \frac{1}{2c^2}(c\tilde{\xi}_{,2} - v_2\kappa) & \frac{1}{2c^2}(c\tilde{\xi}_{,3} - v_3\kappa) & \frac{\kappa}{2c^2} \\ \frac{1}{2c^2}[c^2 + c\frac{V}{A} + \kappa(2e_{\text{kin}} - h)] & -\frac{1}{2c^2}(c\tilde{\xi}_{,1} + v_1\kappa) & -\frac{1}{2c^2}(c\tilde{\xi}_{,2} + v_2\kappa) & -\frac{1}{2c^2}(c\tilde{\xi}_{,3} + v_3\kappa) & \frac{\kappa}{2c^2} \end{bmatrix}$$

[9] Schröder, W., and Hartman, G., "Implicit Solutions of Three-Dimensional Viscous Hypersonic Flows," *Computers and Fluids*, Vol. 21, No. 1, 1992, pp. 109–132. doi:10.1016/0045-7930(92)90036-U

[10] Weiland, C., Schröder, W., and Menne, S., "An Extended Insight into Hypersonic Flow Phenomena Using Numerical Methods," *Computers and Fluids*, Vol. 22, Nos. 4/5, 1993, pp. 407–426. doi:10.1016/0045-7930(93)90016-3

[11] Hänel, D., and Schwane, R., "An Implicit Flux Vector Splitting Scheme for the Computation of Viscous Hypersonic Flow," AIAA Paper AIAA-89-274, Jan. 1989.

[12] Yee, H.C.,"Upwind and Symmetric Shock-Capturing Schemes," NASA TM 89464, NASA Ames Research Center, Moffet Field, CA, May 1987.

[13] Roe, P. L., "Approximate Riemann Solvers, Parameter Vectors and Difference Schemes," *Journal of Computational Physics*, Vol. 43, No. 2, 1981, pp. 357–372. doi:10.1016/0021-9991(81)90128-5

[14] MacCormack, R. W., "The Effect of Viscosity in Hypervelocity Impact Cratering," AIAA Paper AIAA-69-354, 1969; also reprint in *Journal of Spacecraft and Rockets*, Vol. 40, No. 5, 2003, pp. 757–763.

[15] Gottlieb, D., and Turkel, E., "Dissipative 2–4 Methods for Time-Dependent Problems," *Mathematics of Computation*, Vol. 30, No. 136, 1976, pp. 703–723. doi:10.2307/2005392

[16] Ferziger, J. H., *Numerical Methods for Engineering Application*, Wiley, New York, 1981.

[17] Harris, P. J., "Numerical Investigation of Transitional Compressible Plane Wakes," Ph.D. Dissertation, University of Arizona, Tucson, AZ, 1997.

[18] Gross, A., and Fasel, H. F., "High-Order WENO Schemes Based on the Roe Approximate Riemann Solver," AIAA Paper AIAA-2002-2735, June 2002.

[19] Gross, A., and Fasel, H. F., "Chracteristic Ghost-Cell Boundary Condition," *AIAA Journal*, Vol. 45, No. 1, 2007, pp. 302–306. doi:10.2514/1.23130

[20] Kopriva, D. A., "Spectral Solution of the Viscous Blunt-Body Problem," *AIAA Journal*, Vol. 31, No. 7, 1993, pp. 1235–1242.

[21] Sanders, R., Morano, E., and Druguet, M. C., "Multidimensional Dissipation for Upwind Schemes: Stability and Applications to Gas Dynamics," *Journal of Computational Physics*, Vol. 145, No. 2, 1998, pp. 511–537. doi:10.1006/jcph.1998.6047

[22] Suresh, A., and Huynh, H. T., "Accurate Monotonicty-Preserving Schemes with Runge-Kutta Time Stepping," *Journal of Computational Physics*, Vol. 136, No. 1, 1997, pp. 83–99. doi:10.1006/jcph.1997.5745

[23] Sandham, N. D., and Reynolds, W. C., "Compressible Mixing Layer: Linear Theory and Direct Simulation," *AIAA Journal*, Vol. 28, No. 4, 1990, pp. 618–624.

[24] Gustafsson, B., "Convergence Rate for Difference Approximations to Mixed Initial Boundary-Value Problems," *Mathematics of Computation*, Vol. 29, No. 130, 1975, pp. 396–406. doi:10.2307/2005559

[25] Wasistho, B., Geurts, B. J., and Kuerten, J. G. M., "Simulation Techniques for Spatially Evolving Instabilities in Compressible Flow over a Flat Plate," *Computers and Fluids*, Vol. 26, No. 7, 1997, pp. 713–739. doi:10.1016/S0045-7930(97)00021-2

[26] Gross, A., and Fasel, H. F., "Numerical Investigation of Low-Pressure Turbine Blade Separation Control," *AIAA Journal*, Vol. 43, No. 12, 2005, pp. 2514–2525.

[27] Hunt, J. C. R., Wray, A. A., and Moin, P., "Eddies, Stream, and Convergence Zones in Turbulent Flows," *Center For Turbulence Research, Proceedings of the CTR Summer Program*, Stanford Univ., Stanford, CA, 1988, pp. 193–208.

[28] Sondergaard, R., Rivir, R. B., and Bons, J. P., "Control of Low-Pressure Turbine Separation Using Vortex-Generator Jets," *Journal of Propulsion and Power*, Vol. 18, No. 4, 2002, pp. 889–895.

[29] Huang, J., Corke, T., and Thomas, F., "Plasma Actuators for Separation Control of Low Pressure Turbine Blades," AIAA Paper AIAA-2003-1027, Jan. 2003.

X. Zhong
Associate Editor